Polarization and amplitude hybrid modulation of longitudinally polarized subwavelength-sized optical needle

Lijiao Guo (郭丽娇), Changjun Min (闵长俊), Shibiao Wei (魏仕彪), and Xiaocong Yuan (袁小聪)*

Institute of Modern Optics Key Laboratory of Optical Information Science and Technology Ministry of Education of China, Nankai University, Tianjin 300071, China

**Corresponding author: xcyuan@nankai.edu.cn*

Received December 25, 2012; accepted January 28, 2013; posted online April 2, 2013

We present a method of both polarization and amplitude modulations on an incident beam to obtain a longitudinally polarized subwavelength-sized optical needle. A 4-f system with a spatial light modulator is used to generate experimentally a two-mode alternate cylindrical vector beam by polarization modulation, enhancing performance and facilitating implementation. We optimize the beam focusing properties after passing the beam through an annular aperture to obtain amplitude modulation by the simulated annealing algorithm. Numerical results indicate that a sharp focal spot (0.417λ) with a long focal depth (8λ) and a strong longitudinally polarized field can be easily achieved.

OCIS codes: 260.5430, 140.3300.

doi: 10.3788/COL201311.052601.

Focusing an incident beam into a small spot with a long focal depth has received significant research interest in optical engineering[1−5]. The successful generation of radially polarized beams in recent decades provides a basis for obtaining a strong longitudinal field component when it is focused by a high numerical aperture (NA) objective lens. Possible applications in particle acceleration[6], fluorescent imaging[7], second-harmonic generation[8,9], and Raman spectroscopy[10] have been reported. Thus, the generation of a longitudinally polarized beam with a small transverse spot and a long depth of focus (DOF) has drawn considerable interest. For example, a small focal spot with a strong longitudinal component is obtained at the focal region by focusing a radially polarized beam with an extremely narrow annular aperture and a high-NA objective lens[11,12]. An amplitude filter based on Euler transformation can also obtain a longitudinally polarized beam with a long DOF of 9λ, whereas the full-width at half-maximum (FWHM) of the focal spot is 0.8λ[13]. Radially polarized beams combined with a binary phase optical element have efficiently produced a "pure" longitudinally polarized subwavelength beam (also called optical needle) with a DOF of 4λ in high-NA focusing[14−16]. Most previous techniques for manipulating focal depth and size are based on the amplitude or phase modulation of radially polarized beams.

Cylindrical vector beams other than radially polarized beams have been successfully generated and studied in recent years, which allows shaping the focal spot by polarization modulation. In the present study, we propose a method of both polarization and amplitude modulations on the incident beam to obtain an optical needle with a sharp focal spot and a strong longitudinally polarized component. We use a 4-f system comprising a spatial light modulator (SLM) and a common path interferometric arrangement[17,18] to generate directly a two-mode alternate (TMA) cylindrical vector beam by polarization modulation. We use an annular aperture to modulate the amplitude distribution of the TMA beam. A new optimization approach that combines the simulated annealing algorithm[19] and the TMA beam with an annular aperture is proposed to enhance the optimization of beam focusing properties. Optimized results show that the FWHM of the focal spot for the total electric field is 0.417λ; the DOF can be enhanced to 8λ, and the ratio of the longitudinal component to the total electric field for the main-lobe intensity is 0.84.

We firstly investigated the generation of a TMA beam, as shown in Fig. 1. The TMA beam is a type of cylindrical vector beam, with each point having a polarization rotated by ϕ_0 from its radial direction[20]. Different from the radially ($\phi_0 = 0$) and azimuthally ($\phi_0 = \pi/2$) polarized lights, the beam has two modes of polarization in different concentric regions. The beam cross-section is divided into $n$concentric regions ($n = 1, 2, 3, \cdots$), with each region corresponding to a focal angle of $\theta_i (i = 1, 2, \cdots, n)$. As illustrated in Fig. 1, the transverse beam profile of the TMA beam comprises five concentric regions, and each region has the polarization state below:

$$\phi_0 = \begin{cases} 0, & \text{for } 0 < \theta < \theta_1, \theta_2 < \theta < \theta_3, \theta_4 < \theta < \alpha \\ \pi, & \text{for } \theta_1 < \theta < \theta_2, \theta_3 < \theta < \theta_4 \end{cases}, \quad (1)$$

where $\alpha = \arcsin(\mathrm{NA}/n_0)$ represents the maximum focal angle determined by the high-NA objective lens; and n_0 is the refractive index of the surrounding medium.

To generate the TMA beam, we used a 4-f system comprising a SLM and a common path interferometric arrangement[17,18], which is conveniently accomplished by a redesigned computer-generated holographic grating (HG); the experimental setup and HG are shown in Fig. 2. The SLM used was a reflective liquid-crystal display containing 1 920 × 1 080 (pixel) that are 8× 8 (μm)

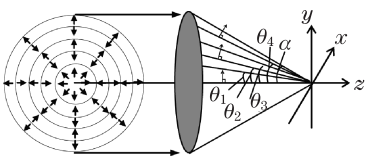

Fig. 1. Focusing layout of a five-region TMA beam. α is the maximum focal angle determined by the high-NA lens.

in size, allowing for precision in HG design. A He–Ne laser beam (λ = 632.8 nm) polarized at 0° to the x-axis illuminates on the SLM and is then diffracted by the HG. Two identical lenses (L_1 and L_2) with a focal length of f are employed in the 4-f system. Only the ±1st orders were allowed to pass through a spatial filter (F) with two separate open apertures placed at the Fourier plane of lens L_1. Two $\lambda/4$ waveplates (Q_1 and Q_2) located at F were used to generate a pair of orthogonal right-handed and left-handed circularly polarized beams. The ±1st-order diffractive beams were recombined by a Damman phase grating (G_1) with a period that matches the HG. G_1exhibits 39% diffraction efficiency for the ±1st-orders, which is much higher than that of a hologram reconstructed either by a SLM or amplitude-modulated diffractive elements. The generated TMA beam is finally recorded by a charge-coupled device camera.

As shown in Fig. 2, the HG can be expressed as $t(x,y) = \frac{2}{\pi}(e^{-i\delta}e^{-i2\pi x f_0} + e^{i\delta}e^{i2\pi x f_0})$, where f_0 is the spatial frequency, and δ is the phase distribution described by $\delta = \varphi + \varphi_0$, with φ and φ_0 representing the azimuth angle and the initial phase, respectively. The HG is divided into five concentric regions with different φ_0 values for five different polarized regions of the TMA beam, equal to 0 and π for odd and even regions, respectively. For a linearly polarized light incident on SLM, its ±1st-order diffracted beams can produce the topological charges of +1 and –1 and then pass through the filter F and the corresponding $\lambda/4$ plate. The ±1st-order beams behind the $\lambda/4$ waveplate can be expressed in the Cartesian coordinate system as $E^{\pm1} = [E_x^{\pm1}, E_y^{\pm}] = (A_0/2)[\exp(\pm j\delta), \mp\mu j\exp(\pm j\delta)]$, where A_0 is a constant factor. The electric field of the recombining beam can be written in a polar coordinate system as $E = E^{+1} + E^{-1} = [E_\rho, E_\varphi] = A_0[\cos(\delta), \sin(\delta)]$, where ρ is the polar radius.

The two-dimensional intensity distribution of the generated TMA beam is shown in the right upper inset of Fig. 2. A dark ring appears in the intensity distribution because of the polarization jump between adjacent regions. The central dark spot originates from the polarization singularity at the beam center. When a linear polarizer (P_2) is used, a bow-tie pattern appears in the intensity distribution because of the cylindrical symmetry of polarization.

We numerically studied the focusing properties of the

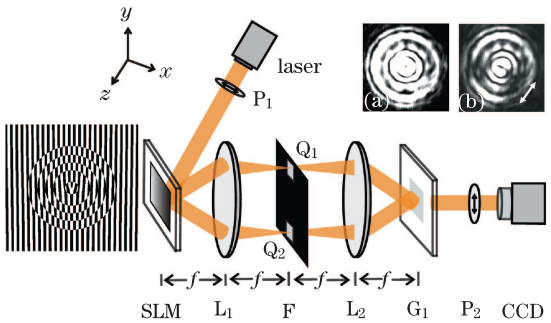

Fig. 2. Schematic of the experimental setup. (Left) Sketch of the holographic grating. (Right upper insets) Experimentally obtained beam intensity distributions (a) without and (b) with a linear polarizer (P_2). The arrow indicates the transmission axis of the linear polarizer.

generated TMA beam and optimized the DOF and FWHM of the focal spot by using the simulated annealing algorithm. According to the vector diffraction theory[20,21], the focal electric field of the TMA beam can be described in a cylindrical coordinate as

$$E_\rho(\rho,z) = \sum_{i=1}^{n} A\cos(\phi_0)\int_{\theta_{i-1}}^{\theta_i} P(\theta)\cos^{1/2} \cdot(\theta)\sin(2\theta)l(\theta)J_1(k\rho\sin\theta)e^{(ikz\cos\theta)}\mathrm{d}\theta, \quad (2)$$

$$E_z(\rho,z) = \sum_{i=1}^{n} 2iA\cos(\phi_0)\int_{\theta_{i-1}}^{\theta_i} P(\theta)\cos^{1/2} \cdot(\theta)\sin^2\theta l(\theta)J_0(k\rho\sin\theta)e^{(ikz\cos\theta)}\mathrm{d}\theta, \quad (3)$$

where $J_0(x)$ and $J_1(x)$ are the 0th and the 1st order Bessel functions of the first kind, respectively; k is the wave number; A is a constant; $P(\theta)$ is an annular pupil apodization function; and $l(\theta)$ describes the amplitude distribution of the incident beam. The focal angle θ_i (i= 1, 2, ⋯, n) for each region corresponds to the radial position r_i= sinθ_i/NA (normalized to the optical aperture). The focal field of the TMA beam can be optimized by changing the focal angles θ_i because of the interference of light from different regions.

The amplitude distribution of the incident Bessel–Gaussian beam is[16]

$$l(\theta) = \exp[-\beta_0^2(\sin\theta/\sin\alpha)^2]J_1(2\gamma_0\sin\theta/\sin\alpha), \quad (4)$$

where $\beta_0 = 1$ and $\gamma_0 = 1$, and J_1 denotes the 1st order Bessel function of the first kind. The NA of the focusing lens is 0.95 and n_0 =1. The annular pupil apodization function can be written as

$$P(\theta) = \begin{cases} 1, & \text{if} \quad \theta_1 \leqslant \theta \leqslant \alpha \\ 0, & \text{otherwise} \end{cases}. \quad (5)$$

Thus, the first central region of the TMA beam is blocked by the annular aperture. The annular aperture was introduced because most E_ρ components of the focus came from the center region of the TMA beam. The beam quality in the focal region was described as the ratio of the longitudinal component (z-direction) to the total field $\eta = \Phi_z/(\Phi_\rho + \Phi_z)$, where $\Phi_i = 2\pi\int_0^{1.5\lambda}|E_i(\rho,0)|^2\rho\mathrm{d}\rho(i=\rho,z)$. The upper limit of the integral of Φ_i was set at 1.5λ, based on the first zero point of the total electric field intensity for the radially polarized beam. The objective is to achieve a focal field with a small FWHM, a long DOF, and a high ratio of η. The parameters of the TMA beam are optimized based on the simulated annealing algorithm[19], which provides a globally optimal solution according to the thermal perturbation theory. The angle of θ_1 was set in the range of no more than 0.6, 0.7, and 0.8α, respectively, in the optimization.

Table 1 presents the DOF, FWHM of the focal spot, ratio η, and conversion efficiency ξ at different optimized focal angles. The table illustrates the performance of the TMA beam with different annular apertures compared with the performance of a conventional radially polarized beam. As a counterpart, the radially polarized beam has a Bessel–Gaussian amplitude distribution. Here, ξ is the

Table 1. Comparison of Key Parameters for TMA Beam with Different Annular Apertures

Focal Angles of TMA Beam (deg.)	DOF (λ)	FWHM (λ)	η	ξ
Radially Polarized Bessel–Gaussian Beam	0.84	0.680	0.45	1
θ_1= 40.79, θ_2= 41.07, θ_3= 44.73, θ_4= 52.71	4.90	0.423	0.83	0.37
θ_1= 43.44, θ_2 =44.66, θ_3 =48.61, θ_4= 55.36	5.25	0.417	0.84	0.30
θ_1= 55.94, θ_2 =56.73, θ_3 =59.74, θ_4 =70.73	8.00	0.417	0.84	0.12

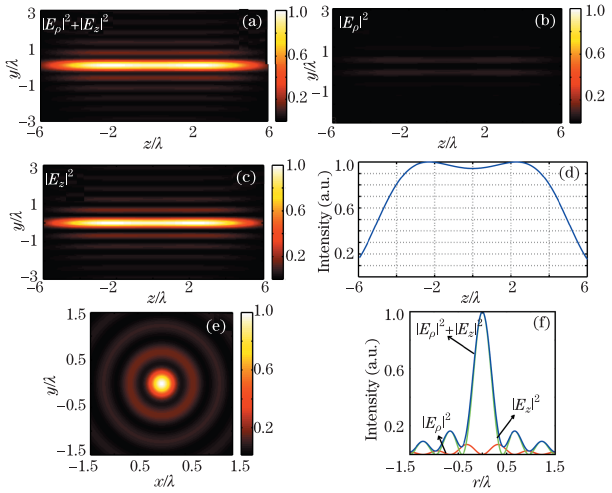

Fig. 3. (Color online) Normalized electric field intensity distributions of the optimized TMA beam with an annular aperture of θ_1= 55.94°. (a) Total electric field, (b) radial component, and (c) longitudinal component intensity distributions in the focal region in the y-z plane. (d) Total electric field intensity distribution in the focal region along the z-axis (y= 0). (e) Contour plot of the total electric field intensity distribution on the focal plane. (f) Electric field intensity distributions in the focal plane in the radial direction.

ratio of the total electric field intensity within the focal volume of a TMA beam with an annular aperture, compared with a radially polarized Bessel–Gaussian beam. When the optimized TMA beam with an annular aperture is focused by a high-NA objective lens, a sharp focal spot with a long DOF and a strong longitudinally polarized component can be achieved. These results are obtained because the interference of light from different polarization regions enhances the E_z component and suppresses the E_ρ component; the annular aperture further reduces the amplitude of the E_ρ component and increases the percentage of the E_z component. With the increase in the inner radius of the annular aperture, the optimized DOF becomes 5.8, 6.25, and 9.5 times longer than that of the radially polarized beam (0.84λ) at θ_1= 40.79°, 43.44°, and 55.94°, respectively. The FWHM values of the focal spot for the total field are 0.423, 0.417, and 0.417λ, which exceed the diffraction limit and are sharper than that of the radially polarized beam (0.68 λ). The optimized ratio $\eta = 0.84$ is nearly twice higher than the radially polarized beam (0.45), resulting in an almost "pure" longitudinally polarized subwavelength beam. However, the ratio of ξ decreases with the increase in the inner radius of the annular aperture because more light is obstructed by the non-transparent center of the annular aperture. Thus, a trade-off between intensity and the size of focus occurs.

The intensity distributions of the total, radial, and longitudinal fields at the axial cross-section for the TMA beam with an annular aperture of θ_1= 55.94° are shown in Figs. 3(a)–3(c), respectively. The intensity of the E_ρ component becomes markedly smaller than that of the E_z component after optimization. The axial electric field intensity is observed to be uniform, and the generated beam is non-diffracting over a long range of 8λ. These findings can also be inferred from the electric field intensity profile shown in Fig. 3(d). The calculated total electric field intensity distribution in the focal plane is shown in Fig. 3(e). The FWHM of the focal spot for the total field is measured at 0.417λ, as shown in Fig. 3(f), which is a sub-diffraction-limited result and remains sharper than that of the radially polarized beam. Figure 3(f) also shows that the maximum intensity for all sidelobes are lower than 0.2, and the ratio of η is as high as 0.84.

In conclusion, we propose a method of both polarization and amplitude modulations on the incident beam to achieve an optical needle with a sharper focal spot and stronger longitudinally polarized component. We use a 4-f system to generate experimentally a TMA cylindrical vector beam. We also optimize the focusing properties of the TMA beam by using an annular aperture and the simulated annealing algorithm. Optimized results show that a sharp focal spot (0.417λ) with a long DOF (8λ) is achieved and the longitudinally polarized component is enhanced. This study has potentials applications in focus resolution enhancement.

This work was supported by the National Natural Science Foundation of China (Nos. 61036013, 61138003, and 11204141). X. C. Yuan acknowledges the support given by Tianjin Municipal Science and Technology Commission (No. 11JCZDJC15200). C. J. Min acknowledges the support provided by Tianjin Municipal Science and Technology Commission (No. 12JCYBJC31000).

References

1. N. Davidson, A. A. Friesem, and E. Hasman, Opt. Lett. **16,** 523 (1991).
2. H. F. Wang, L. P. Shi, G. Q. Yuan, X. S. Miao, W. L. Tan, and T. C. Chong, Appl. Phys. Lett. **89,** 171102 (2006).
3. Y. S. Xu, J. Singh, C. J. R. Sheppard, and N. G. Chen, Opt. Express **15,** 6409 (2007).
4. G. H. Yuan, S. B. Wei, and X.-C. Yuan, Opt. Lett. **36,** 3479 (2011).
5. G. H. Yuan, S. B. Wei, and X.-C. Yuan, J. Opt. Soc. Am. A **28,** 1716 (2011).
6. Q. W. Zhan, Opt. Express **12,** 3377 (2004).
7. L. Novotny, M. R. Beversluis, K. S. Youngworth, and T.

G. Brown, Phys. Rev. Lett. **86,** 5251 (2001).
8. A. Bouhelier, M. Beversluis, A. Hartschuh, and L. Novotny, Phys. Rev. Lett. **90,** 013903 (2003).
9. D. P. Biss and T. G. Brown, Opt. Lett. **28,** 923 (2003).
10. N. Hayazawa, Y. Saito, and S. Kawata, Appl. Phys. Lett. **85,** 6239 (2004).
11. R. Dorn, S. Quabis, and G. Leuchs, Phys. Rev. Lett. **91,** 233901 (2003).
12. S. Quabis, R. Dorn, M. Eberler, O. GlÖckl, and G. Leuchs, Opt. Commun. **179,** 1 (2000).
13. J. Lin, K. Yin, Y. D. Li, and J. B. Tan, Opt. Lett. **36,** 1185 (2011).
14. C. Sun and C. K. Liu, Opt. Lett. **28,** 99 (2003).
15. H. F. Wang, L. P. Shi, B. Lukyanchuk, C. Sheppard, and C. T. Chong, Nat. Photon. **2,** 501 (2008).
16. K. Huang, P. Shi, X. L. Kang, X. B. Zhang, and Y. P. Li, Opt. Lett. **35,** 965 (2010).
17. X. L. Wang, J. P. Ding, W. J. Ni, C. S. Guo, and H. T. Wang, Opt. Lett. **32,** 3549 (2007).
18. L. J. Guo, C. J. Min, G. H. Yuan, C. L. Zhang, J. G. Wang, Z. Shen, and X.-C. Yuan, Opt. Express **20,** 24748 (2011).
19. S. Kirkpatrick, C. D. Gelatt, and M. P. Vecchi, Science **220,** 671 (1983).
20. K. S. Youngworth and T. G. Brown, Opt. Express **7,** 77 (2000).
21. Q. W. Zhan and J. R. Leger, Opt. Express **10,** 324 (2002).